Cell Reports
Physical Science

CellPress
OPEN ACCESS

Article

Thermodynamics-driven interfacial engineering of alloy-type anode materials

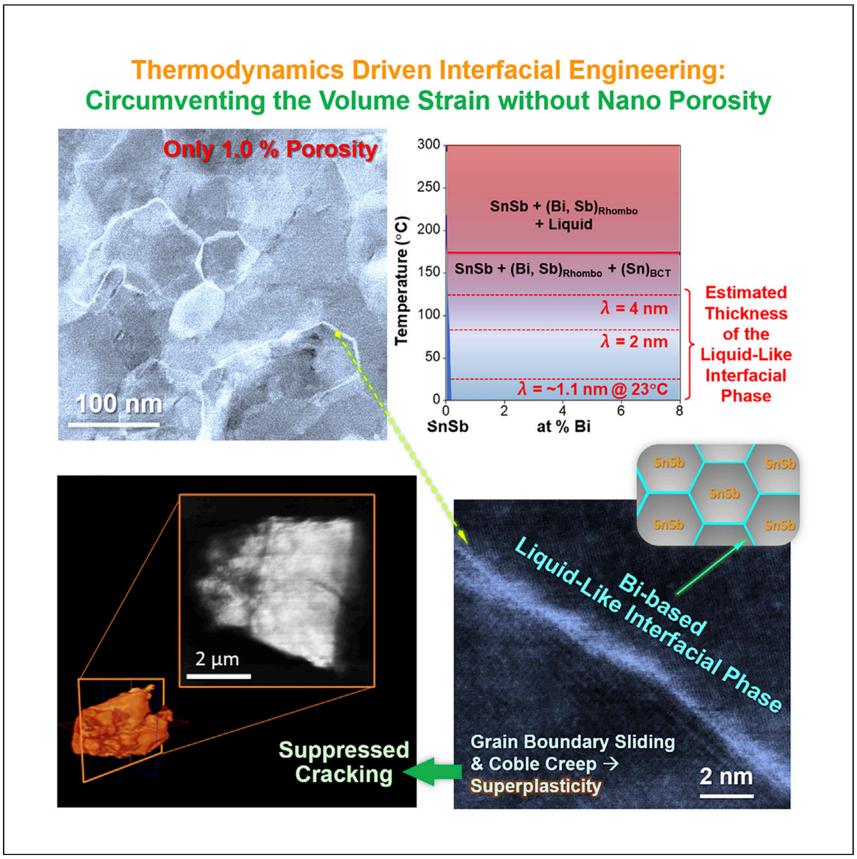

Alloy-type anodes are promising for Li-ion batteries, but the large volume change during electrochemical cycling can cause fast degradation. Yan et al. report a thermodynamics-driven interfacial engineering method to improve alloy-type anodes via the spontaneous formation of liquid-like interfacial phase that promotes room temperature superplasticity to alleviate cracking.

Qizhang Yan, Shu-Ting Ko, Andrew Dawson, ..., Johanna Nelson Weker, Sarah H. Tolbert, Jian Luo

jluo@alum.mit.edu

Highlights

Spontaneously formed liquid-like interfacial phase improves the SnSb-Bi anode

Cryogenic STEM reveals Bi segregation at SnSb grain boundaries

Transmission X-ray microscopy shows the suppressed cracking upon cycling

Liquid-like interfacial phase promotes grain boundary sliding and Coble creep

Yan et al., Cell Reports Physical Science *3*, 100694
January 19, 2022 © 2021 The Author(s).
https://doi.org/10.1016/j.xcrp.2021.100694

Cell Reports
Physical Science

CellPress
OPEN ACCESS

Article

Thermodynamics-driven interfacial engineering of alloy-type anode materials

Qizhang Yan,[1] Shu-Ting Ko,[2] Andrew Dawson,[3] David Agyeman-Budu,[5] Grace Whang,[4] Yumin Zhao,[1] Mingde Qin,[1] Bruce S. Dunn,[4] Johanna Nelson Weker,[5] Sarah H. Tolbert,[3,4] and Jian Luo[1,2,6,*]

SUMMARY

Alloy-type anodes can enable high specific capacity for Li-ion batteries, but the large volume change during cycling often causes fast-capacity fading. Here, we report a thermodynamically driven grain boundary engineering method to improve alloy-type anodes via the spontaneous formation of 2D interfacial phases (complexions). Notably, the 2.8 at% Bi-doped SnSb achieves improved cycling stability and rate capability, even though it is 99% dense and has a mean crystallite size 2.7× larger than the undoped SnSb reference sample. Cryogenic transmission electron microscopy reveals Bi segregation at grain boundaries. Thermodynamic modeling further suggests the stabilization of a nanoscale liquid-like interfacial phase. Synchrotron transmission X-ray microscopy shows the suppressed intergranular cracking upon cycling with Bi addition. It suggests that the liquid-like interfacial phase serves as a stress relief mechanism for the high volumetric expansion anode via improved grain boundary sliding and Coble creep, akin to room-temperature superplasticity observed in Sn-Bi.

INTRODUCTION

Lithium-ion batteries (LIB) have become one of the main energy storage solutions for our modern society.[1,2] However, the current generation batteries cannot satisfy the fast-growing demand for energy density. The theoretical capacity of graphite, 372 mAh/g or 756 Ah/L, is one of the limitations to achieving high battery–energy density, and this drives researchers to study alternative options. Li-alloying reactions with various metal and intermetallic compounds (such as Si, Sn, and SnSb) have attracted recent research attention because of their high specific capacities.[3,4] However, the cycling stability of alloy-type anodes is typically poor due to the high volumetric changes during lithiation and delithiation. For example, Sn can expand by more than 300% after complete lithiation.[5] During the lithiation process, the expanded lithiated phase from the particle surface generates high compressive stress on large particles.[6,7] For micron-sized Sn particles, the surface hoop tension can cause crack nucleation and propagation. During the delithiation process, void channels were also found to form within the particle through percolation dissolution.[8–10] Electrolyte decomposition can repeatedly occur on the newly exposed electrode surfaces, which leads to continuous solid electrolyte interphase (SEI) growth.[11] Fractured fragments of active material can also become electrically isolated, causing capacity decay.

To overcome these challenges, various strategies have been proposed in past studies, including carbon/metal composites,[12–15] nanoporous structures,[5,16,17]

---

[1]Department of Nanoengineering, University of California San Diego, La Jolla, California 92093, United States

[2]Program of Materials Science and Engineering, University of California San Diego, La Jolla, California 92093, United States

[3]Department of Chemistry and Biochemistry, University of California Los Angeles, Los Angeles, California 90095, United States

[4]Department of Materials Science and Engineering, University of California Los Angeles, Los Angeles, California 90095, United States

[5]Stanford Synchrotron Radiation Lightsource, SLAC National Accelerator Laboratory, Menlo Park, California 94025, United States

[6]Lead contact

*Correspondence: jluo@alum.mit.edu

https://doi.org/10.1016/j.xcrp.2021.100694

novel binders/electrolyte additives,[18–20] and surface coatings[21–23]. For cycling stability improvements, a second metal species can be introduced. For example, SnSb lithiates via a two-step reaction: Sb first reacts with Li^+ at ~0.8 V to form a Li_3Sb matrix; then Sn starts to lithiate at 0.7 V. The two-step reaction can alleviate the strain upon lithiation,[24] but the micrometer-sized SnSb can still crack during cycling, resulting in fast, irreversible capacity decay.[25]

Kinetically controlled interfacial engineering, particularly various surface coating methods, have been widely used to improve alloy electrode cycling stability.[3] Generally, coatings can act as a barrier to stabilize the electrochemical interface. For example, Kohandehghan et al.[26] discovered 3-nm Sn coating on Si nanowires made by physical vapor deposition can improve cycling stability. The compressive stress from the lithiated Sn coating can confine the radial expansion of the Si nanowires. Ye et al.[27] showed that atomic layer deposition of Al_2O_3 and TiO_2 on Si micropillars led to thinner SEI and enhanced structural stability. To date, most interfacial engineering studies focus on surface modification and utilize kinetically controlled coatings. In contrast, grain boundary (GB) engineering has not been widely investigated. Moreover, thermodynamically driven interfacial engineering has emerged as a new route to tailor batteries,[28] which has not yet been applied to alloy-type anodes.

Here, we use the GB segregation of Bi and the associated spontaneous formation of a liquid-like interfacial phase to improve the performance SnSb Li-ion battery anodes. Bi is selected as the GB modification element with the following considerations: (1) The Sn-Sb-Bi ternary system has limited solubility of Bi in SnSb,[29,30] suggesting GB segregation of Bi. (2) Sn-Bi alloys have been reported to show superplasticity, with stable elongation up to ~1950% under tensile stress at room temperature.[31,32] We hypothesize that Bi-segregated SnSb GBs can stabilize the grain structure upon cycling as well as enabling stress release through GB sliding and Coble creep in a mechanism akin to the room-temperature superplasticity observed in Sn-Bi.[31,32] We add 2.8 at% (5 wt%) Bi to SnSb and confirm the Bi segregation at SnSb GBs using cryogenic scanning transmission electron microscopy (cryo-STEM). Notably, this method can substantially improve the SnSb cycling stability and rate capability, even though the addition of Bi leads to dense micrometer-sized secondary particles with only 1% porosity, thereby pointing to a new direction of thermodynamics-driven interfacial engineering.

RESULTS

Synthesis and characterization

Thermodynamics-driven interfacial engineering can be achieved via a facile ball milling and annealing method. Samples with 48.6 at% Sn, 48.6 at% Sb, and 2.8 at% of Bi were first planetary ball milled for 8 h, and then annealed at 250°C under Ar for 3 h. A benchmark SnSb specimen was processed using the same method, but without Bi, for comparison. Figure S1B shows the XRD patterns of the SnSb and SnSb+Bi alloy anodes. The diffraction peaks could be indexed with SnSb (ICSD-154085) in the $R\overline{3}m$ space group for both samples. Since only 2.8 at% of Bi was added, diffraction peaks from Bi could not be observed in the SnSb+Bi specimen. The solid solubility limit of Bi in SnSb is < 2 at% at room temperature;[29,30] thus, the extra Bi should be located at GBs and triple-grain junctions.

The averaged as-synthesized (secondary) particle sizes of SnSb and SnSb+Bi were both about 3 μm, as shown in Figures 1A, 1D, and S2. We note that each of the

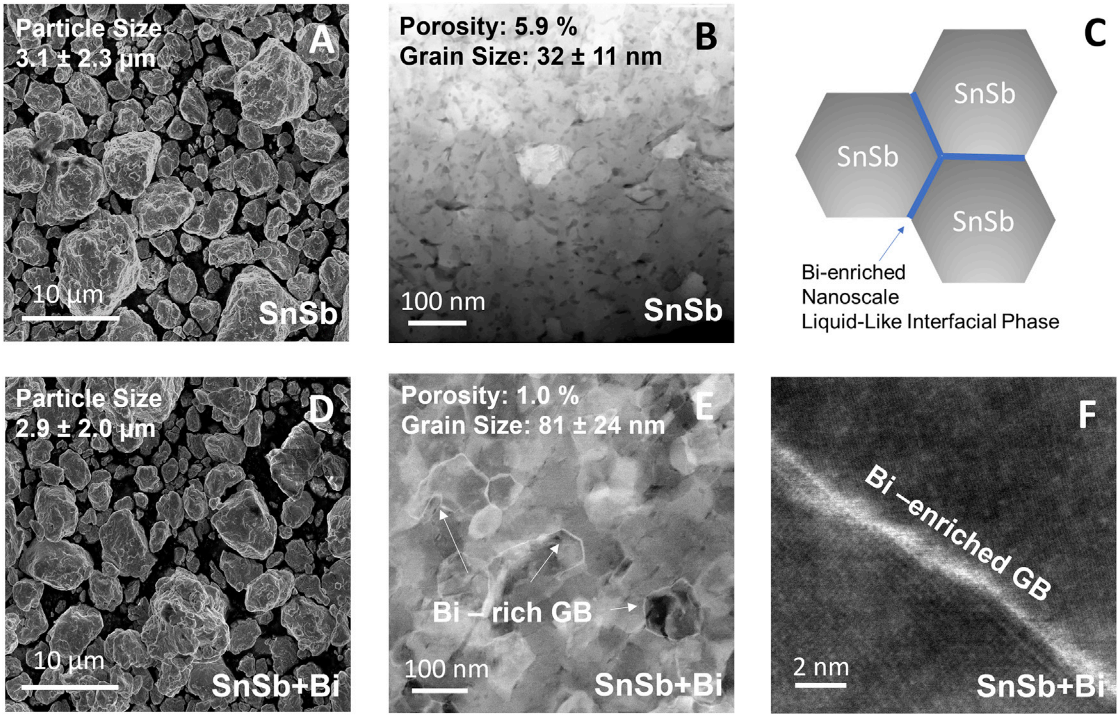

Figure 1. Scanning electron microscopy and cryogenic scanning transmission electron microscopy micrographs of the SnSb and SnSb+Bi anode materials

(A–F) SEM images of (A) SnSb and (D) SnSb+Bi particles shows similar secondary particle diameters. High-angle annular dark-field (HAADF) cryo-STEM images of (B) SnSb and (E) SnSb+Bi, where the bright contrast at grain boundaries (GBs) in the latter indicates the formation of a Bi-rich interfacial phase. (F) High-magnification HAADF cryo-STEM image showing bright contrast at GBs indicating Bi segregation in the SnSb+Bi specimen. STEM specimens were imaged at cryogenic temperatures, which is essential to prevent beam damage (melting) of the specimens. (C) A schematic diagram of the SnSb+Bi grain structure.

secondary particle consisted of many crystalline grains and a small fraction of pores. Figures 1B, 1E, and S4 show cryo-STEM images of SnSb and SnSb+Bi. The SnSb sample showed an averaged grain size of 32 ± 12 nm and ~6% porosity (Figures S3B and S3C). In contrast, the sample with Bi showed an averaged grain size of 81 ± 12 nm (Figure S3F), which was more than doubled the grain size of the undoped SnSb annealed under the same conditions. Moreover, the SnSb+Bi sample showed less porosity (only ~1%), as shown in Figure S3E. Overall, the addition of 2.8 at% Bi led to an ~2.7 × increase in grain size with a substantially reduced porosity, while the same secondary particle size of 2 μm and morphology were maintained. These differences can be explained by the presence of a Bi-enriched liquid interfacial phase at the annealing temperature of 250°C (Figure S5), which led to liquid-phase sintering and grain growth.

Given the low melting point of the Bi-rich interfacial phase, cryo-STEM was used to prevent/reduce damage of specimens by electron beam at high magnifications. The specimens were kept at approximately − 170°C during cryo-STEM imaging. We note that the calculated phase diagram based on National Institute of Standards and Technology (NIST) database[33] (Figure S16) suggests no phase transformation for SnSb + 2.8 at. % Bi below room temperature. Moreover, we believe that the Bi-enriched liquid-like interfacial structure can be quenched to the cryogenic temperature for scanning transmission electron microscopy (STEM) characterization. For the SnSb+Bi sample, bright contrast was observed at GBs in the high-angle annular dark-field image (HAADF) shown in Figure 1E. The Z contrast can be

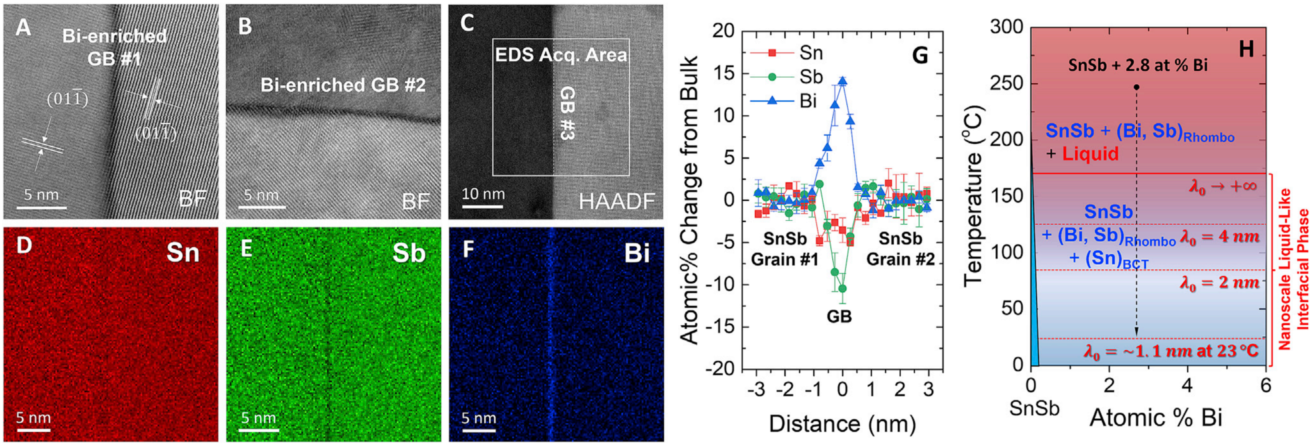

Figure 2. Cryo-STEM energy dispersive X-ray spectroscopy elemental maps of a SnSb+Bi grain boundary and thermodynamic modeling

(A and B) High-magnification cryo-STEM BF images of SnSb+Bi GBs.

(C–F) (C) Cryo-STEM HAADF image of a SnSb+Bi GB and the EDS acquisition area. EDS elemental maps for (D) tin, (E) antimony, and (F) bismuth (in atomic percentages).

(G) Line profile across the GB showing the changes in the atomic percentages of Sn, Sb, and Bi with respect to the bulk composition. This GB structure can be considered as a nanoscale, Bi-enriched, liquid-like, interfacial phase. The error bar represents standard deviation over three measurements.

(H) A computed GB λ diagram,[34–37] where red dashed lines (computed λ_0 values) are plotted in the bulk isopleth of SnSb + x at% Bi to represent the (upper bound of) estimated thickness of a liquid-like interfacial phase that can be thermodynamically stabilized at an average general GB. Note that $\lambda_0 \rightarrow \infty$ at T_S = ~172°C, where a bulk liquid phase appears.

See Note S1 for the underlying interfacial thermodynamic model and calculation procedure.

correlated to atomic number in HAADF; therefore, Figure 1E indicates Bi segregation at GBs. In comparison, such bright contrast was not observed at the SnSb GBs (Figure 1B). Note that grain boundaries exhibit different contrasts in Figure 1E. This is because the five macroscopic (crystallographic) degrees of freedom of the grain boundaries result in significant boundray-to-boundary variation in a polycrystal. In addition, the boundaries can be at different angles with the electron beam in STEM, thereby affecting their contrasts and apparent widths in the projected images.

To quantitatively evaluate the GB segregation at 250°C, a dense SnSb pellet with 2.8 at% of Bi was fabricated. This dense pellet allows the sample to have larger grain sizes, which are needed for quantitative GB elemental characterization in an edge-on geometry in STEM, while maintaining the same heat treatment temperature profile used to produce the electrode powder. The high-resolution bright-field (BF) image in Figure 2A shows an interplanar spacing of 0.307 nm for both grains, which corresponds to the (01$\bar{1}$) planes of SnSb. Dark contrast was observed at GBs in the BF images, indicating Bi segregation at the SnSb GB (Figures 2A and 2B). Cryo-STEM energy dispersive X-ray spectroscopy (EDS) was also carried out to determine the GB element composition. As shown in Figure 2C, the EDS acquisition area was placed between two SnSb grains that have different zone axis. Figures 2D–2F show the atomic percentage mapping of Sn, Sb, and Bi, respectively. There are decreases in intensities for Sn and Sb at the GB and obvious increased contrast for Bi at GB. Cryo-STEM EDS maps of three other GBs randomly selected from the dense SnSb+Bi pellet are shown in Figure S15. All three GBs showed Bi enrichments. The composition of Sn, Sb, and Bi was extracted from the EDS elemental map as shown in Figure 2G. Bulk SnSb+Bi grain composition was measured to be 48.1 at % Sn, 49.3 at% Sb, and 2.6 at% Bi (Figure S12). The composition of the bulk grain was then set as the reference, and atomic composition change was plotted against the distance from the GB. Bi composition increased by ~15% at the GB compared to bulk regions, while Sn and Sb decreased by ~5% and ~10%, respectively. The chemical width (full width half maximum) of the Bi-rich interfacial phase measured from EDS profile was 0.9 ± 0.1 nm thick (Figure 2G). The nominal composition at the center of the GB was measured to have 44.6 at% Sn, 38.9 at% Sb, and 16.5 at% Bi. However, this measured elemental composition has some contributions from the bulk grains due to the beam smearing effects and slight deviation from the exact edge-on condition. Thus, the GB core is likely more enriched with Bi (and more depleted with Sb).

Calculation of phase diagram (CALPHAD) simulations based on a NIST database[33] (Figure S5) suggests the formation of a small fraction of (< 3 at%) a Bi-enriched liquid phase in the SbSn+Bi materials at the annealing temperature of 250°C (Figures 2H and S5C). This bulk liquid phase vanishes at the solidus temperature T_S = ~172°C via a ternary invariant reaction: SnSb + Liquid → $(\text{Bi, Sb})_{\text{Rhombo}}$ + $(\text{Sn})_{\text{BCT}}$. This bulk liquid phase is enriched in Bi and depleted in Sb (43.8 at% Bi and 1.4 at% Sb at T_S); this is coincident with the observed GB composition (Figure 2G), thereby suggesting that at least the GB composition is "liquid-like." Further calculations using an interfacial thermodynamic model taken from prior studies[34–38] suggested that the nanoscale, Bi-enriched, liquid-like, interfacial phase can be stabilized below the bulk solidus temperature (with the interfacial width scaled by the computed λ_0 values in the Figure 2H). This model will be introduced in the Discussion section and further elaborated in Note S1. Such a liquid-like interfacial structure can presumably promote GB sliding and Coble creep to mitigate cracking during cycling, as we will discuss later.

Electrochemical performance

Annealed SnSb and SnSb+Bi powder after ball milling was first examined using galvanostatic cycling at a current density of 100 mA/g, as shown in Figure S1A. The SnSb electrode showed severe capacity decay and only retained 26% capacity after 40 cycles. The Coulombic efficiency also quickly decays to 94% after 20 cycles, indicating poor cycling stability and sustained irreversible reactions. After 2.8 at% Bi was added to the SnSb, the capacity retention increased to 84% after 40 cycles with an averaged Coulombic efficiency of 97.8 ± 0.2%. This demonstrates that the addition of small amounts of Bi to SnSb can significantly improve electrode cycling performance.

The cycling performance of the SnSb+Bi anodes can be further improved. Recent research on alloy-type anodes has shown that a carbon composite structure can enhance cycling stability.[39,40] Building on those results, 6.2 wt% of graphite was planetary ball milled with both SnSb and SnSb+Bi to fabricate carbon composite anodes, [SnSb]-C and [SnSb+Bi]-C. The composite anodes were also annealed at 250°C for 3 h. Figures 3A and S14 show the cycling stability of the carbon composite electrodes. The [SnSb]-C composite delivered a capacity of 60 ± 40 mAh/g after 200 cycles, retaining only around 9% of its initial charge capacity. In contrast, the [SnSb+Bi]-C composite demonstrated improved cycling stability. A capacity of 570 ± 4 mAh/g was maintained after 200 cycles, which corresponds to around 86% capacity retention. Figures 3B and 3C compare the charge and discharge curves of [SnSb]-C and [SnSb+Bi]-C composite anodes. The first cycle discharge capacity for both electrodes are around 835 mAh/g, which includes the initial irreversible capacity from the formation of the SEI layer. Severe capacity decay and voltage hysteresis was observed for the SnSb carbon composite anode. In comparison, the [SnSb+Bi]-C sample showed almost no capacity decay after 150 cycles. The rate capabilities of the [SnSb]-C and [SnSb+Bi]-C carbon composite samples are shown in

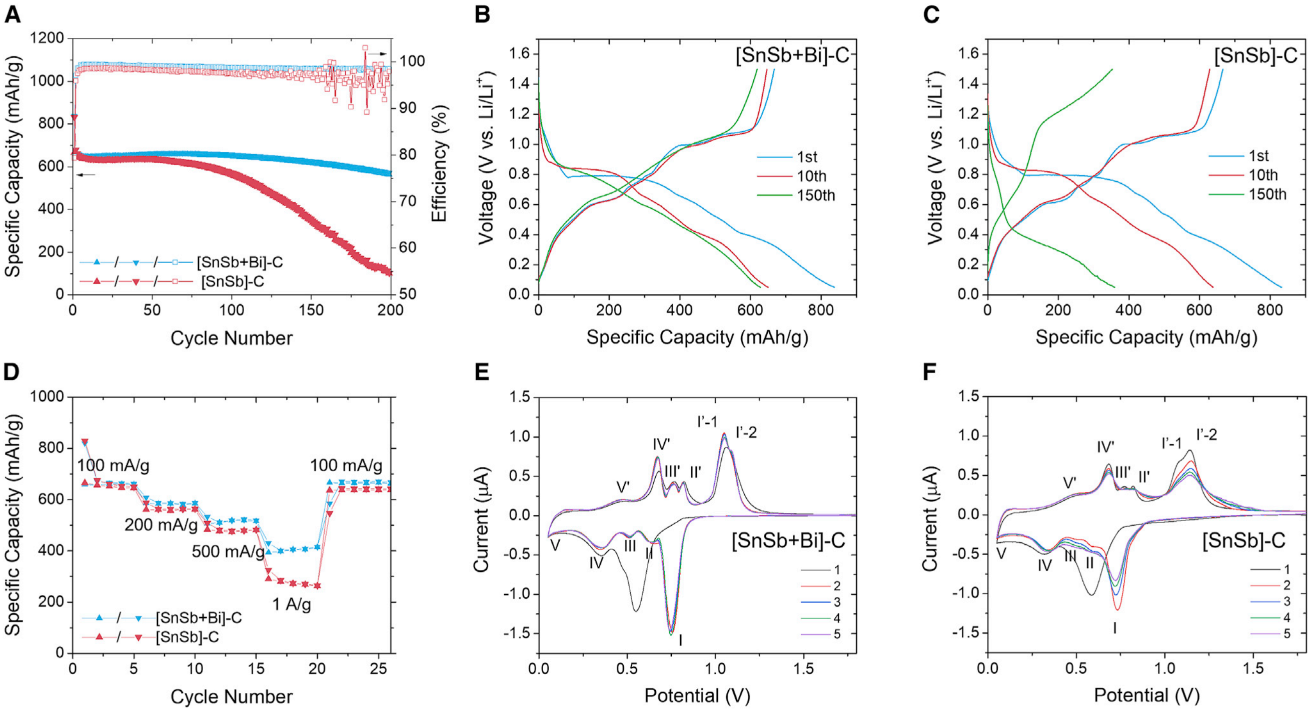

Figure 3. Electrochemical characterization of the [SnSb]-C and [SnSb+Bi]-C composite anodes

(A) Cycling stability comparison for the [SnSb]-C and [SnSb+Bi]-C composite anodes cycled at 100 mA/g between 0.05-1.5 V versus Li/Li$^+$. Here, the up-pointing triangles represents charge specific capacity, the down-pointing triangles represents discharge specific capacity, and the hollow squares represents the Coulombic efficiency.

(B and C) (C) [SnSb+Bi]-C and (C) [SnSb]-C composite anode for the 1st, 10th, and 150th cycle at 100 mA/g.

(D–F) (D) Rate capability comparison of [SnSb]-C and [SnSb+Bi]-C composites samples. Cyclic voltammograms of (E) [SnSb+Bi]-C and (F) [SnSb]-C composite anodes for 5 cycles at 0.1 mV/s between 0.05 and 1.5 V versus Li/Li$^+$.

Figure 3D. At a higher current density of 200 mA/g, 500 mA/g, and 1 A/g, the [SnSb+Bi]-C sample demonstrated charge capacities of 585 mAh/g, 520 mAh/g, and 410 mAh/g, respectively, which corresponds to 89%, 79%, and 62% retention of the 100 mA/g capacity, respectively. In contrast, the [SnSb]-C sample showed decreased charge capacities of 558 mAh/g, 473 mAh/g, and 270 mAh/g, respectively, which corresponds to 85%, 72%, and 41% retention of the 100 mA/g capacity.

To further study the reaction kinetics of the two electrodes, cyclic voltammetry (CV) profiles were compared for 5 cycles at a sweep rate of 0.1 mV/s (Figures 3E and 3F). During the first CV cycle, a strong reduction peak at ~0.5 V was observed for both electrodes. This peak is attributed to the formation of the SEI layer, as well as the lithiation reactions of SnSb to form Li_3Sb, Li_2Sn_5, and LiSn. This first cycle peak shift and convolution due to SEI formation was also reported in previous studies of the Sn- and Sb-based systems.[41–44] The redox reactions of SnSb can be identified from Cycle 2 to Cycle 5, which are labeled as I–V in the CV plot. Based on the phase diagram and recent studies,[3,45–48] lithiation reactions lead to the formation of (I) Li_3Sb and Sn, (II) Li_2Sn_5, (III) LiSn, (IV) Li_5Sn_2, and (V) $Li_{22}Sn_5$ in a sequence. Upon delithiation, a series of reactions lead to the formation of (V′) Li_5Sn_2, (IV′) LiSn, (III′) Li_2Sn_5, (II′) Sn, (I′-1) SnSb, and (I′-2) Sb. The detailed reaction formulae are shown in Figure S17. In Figure 3F, the [SnSb]-C electrode showed a significant current decay with increasing cycle number, indicating increased irreversible capacity upon cycling. In comparison, the redox peak currents for the [SnSb+Bi]-C electrode in Figure 3E were primarily unchanged from Cycle 1 to 5,

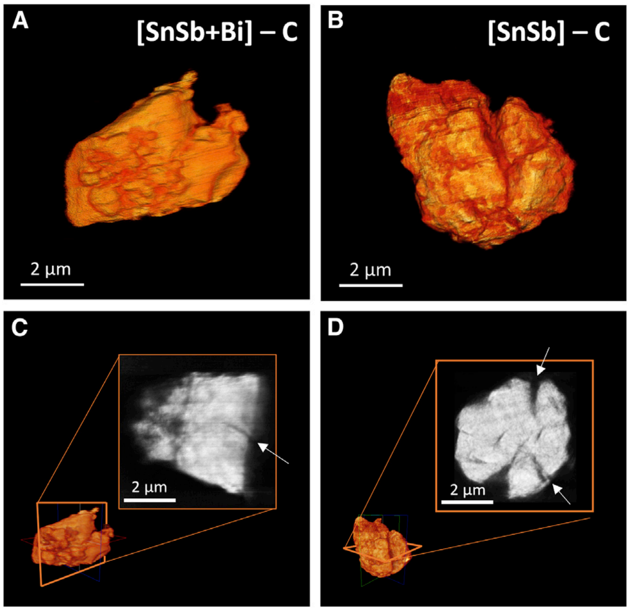

Figure 4. 3D X-ray tomographic reconstruction of the [SnSb]-C and [SnSb+Bi]-C composite anodes after 20 cycles

(A–D) 3D X-ray tomographic reconstructions of a single secondary particle from (A) [SnSb+Bi]-C and (B) [SnSb]-C composite anodes after 20 cycles down to 0.05 V versus Li/Li^+. Cross-section slices of a secondary particle from (C) [SnSb+Bi]-C and (D) [SnSb]-C composite anodes after 20 cycles down to 0.05 V versus Li/Li^+. Cracks are indicated with white arrows. Post-cycling SEM and TXM images at different locations can be found in Figures S7–S9.

showing improved cycling stability. When the scan rate increased from 0.1 mV/s to 0.8 mV/s (shown in Figure S17), the peak shape of the [SnSb+Bi]-C electrode was preserved. At 0.8 mV/s, the peak separation of the redox couple I–I′ for the [SnSb+Bi]-C electrode was 0.66 V, which was noticeable smaller than the [SnSb]-C electrode (0.78 V). This suggests a faster reaction kinetics after Bi addition.[49,50]

Overall, SnSb+Bi anodes showed significantly enhanced cycling stability and rate capability, in comparison to the pure SnSb. The carbon composite version of [SnSb+Bi]-C achieved superior performance with ~86% capacity retention after 200 cycles at 100 mA/g. This is a notable (and somewhat surprising) result, given that Bi doped SnSb is denser (with only 1% porosity inside the particle) than the pure SnSb and its mean primary grain size is 2.7 × larger (~81 nm versus ~32 nm). In conventional theory, a higher porosity and a smaller crystallite size are preferred for alleviating the volume change during cycling for alloy-type anode.

Transmission X-ray microscopy characterization

To understand the role of Bi in improving cycling stability, 3D *ex situ* transmission X-ray microscopy (TXM) and 2D *in situ*/operando TXM were performed at the Stanford Synchrotron Radiation Lightsource (SSRL) beamline 6-2. Alloy particles were imaged after 20 cycles at a current density of 100 mA/g, cycled between 0.05-1.5 V versus Li/Li^+. Figures 4A and 4B show the volume renderings of a primary particle from an [SnSb+Bi]-C and an [SnSb]-C composite after cycling, respectively. Figures 4C and 4D show the corresponding cross-sectional slices. Both surface radial cracks and internal cracks (indicated with arrows) were observed for the [SnSb]-C composite particles after 20 cycles. 2D TXM images (Figures S9D–S9F) and SEM images (Figures S6 and S8) of [SnSb]-C composite particles also showed major cracks, especially for the particles >5 μm in diameter. This indicates that the Li ion diffusion and phase transformation induced stresses surpass the yield stress of the material. Moreover, images from the cycled [SnSb]-C electrodes showed large bumps protruding from the particle surface due to volume expansion (Figure S8), further increasing reaction sites for the formation of excessive SEI. For the [SnSb+Bi]-C composite electrode, SEM images showed only minor bulges from the particle surface after 20 cycles, according to Figure S7, and no severe cracking was observed for particles < 2 μm diameter (Figures S7, S9A, S9B, and S9C). For particles >5 μm in diameter, minor cracks still form, as shown in the cross-sectional slice in Figures 4C, S7E, and S7F post-cycling SEM images. Nevertheless, most particle shapes were maintained, and no severe fracture was observed.

The morphology difference of these cycled powders can also help to explain the differences in cycling stability. The Coulombic efficiency of the [SnSb+Bi]-C anode reached ~99.5% after five cycles, suggesting that only minor electrolyte decomposition occurs on the anode particles at the initial cycles. For the [SnSb]-C anode, the Coulombic efficiency was 98.5% at the 20th cycle. This indicates that newly exposed anode surfaces continuously lead to electrolyte decomposition reaction and subsequently decrease the Coulombic efficiency. The specific capacity for the [SnSb]-C anode was 631 mAh/g after 20 cycles. From 70th to 150th cycles, the specific capacity rapidly decayed from 622 mAh/g to 355 mAh/g, which indicates that the cracking observed in TXM eventually causes the particle to pulverize and that the fractured fragments become electrically isolated. Previous *in situ* TEM[51] and TXM studies[52] have shown that electrical isolation of fractured particles is one of the major capacity degradation mechanisms for alloy-type anodes.

Figure 5 shows the *in operando* 2D TXM of [SnSb+Bi]-C composite during the first lithiation and delithiation cycle. Li metal pouch cells were assembled with a [SnSb+Bi]-C composite electrode as the cathode. Low active material and high conductive carbon mass loading electrodes were used to prevent particle overlapping. Figure 5B shows the pristine particle morphology. The areal expansion of individual particle (average over three particles) was calculated and is shown in Figure 5A; the full set of *in operando* 2D TXM images are shown in Figures S10 and S11. For the SnSb initial lithiation reaction to form Li_3Sb and Sn at 0.8 V, the particle showed ~25% areal expansion. The expansion rate decreased after the first plateau until full lithiation and finally reached ~40% areal expansion. This corresponds to ~65% volume expansion, assuming the particle expands uniformly in all directions. In contrast, the particle area stayed relatively constant during delithiation with no apparent volume shrinking. Overall, no major cracks were observed during this first cycle for all the imaged particles (Figures 5C and 5D). This further verifies the effect of Bi addition on microstructure stabilization upon lithiation and delithiation.

DISCUSSION

The Bi-enriched GB configuration (Figures 1E and 2) can be considered as the metallic counterpart to the well-known nanoscale intergranular films (IGFs) in ceramics initially identified by Clarke[53] or the "nanolayer" in the "Dillon-Harmer complexion" series[54]. Such intergranular films can generally be understood to be liquid-like interfacial phases that possess an equilibrium thickness,[53,55] which are thermodynamically 2D phases[54]. Notably, such nanoscale liquid-like interfacial phases can also be stabilized below the bulk solidus temperatures, in both ceramics

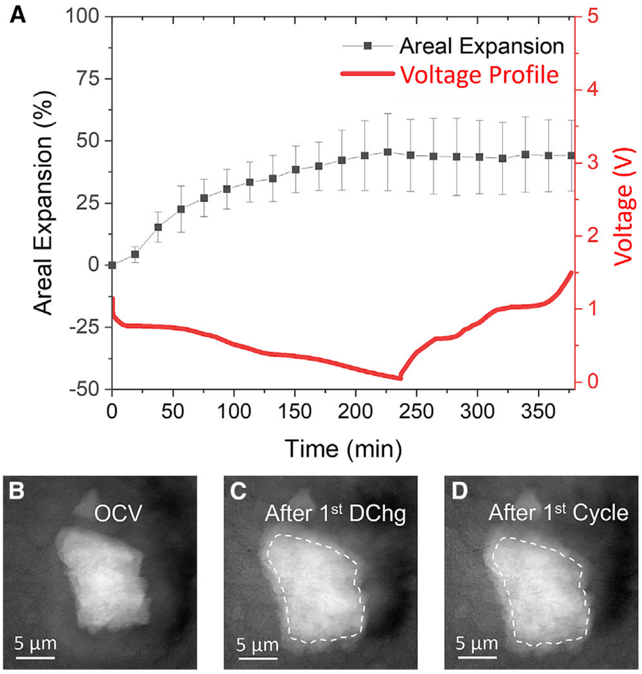

Figure 5. *In situ* 2D TXM characterization of a [SnSb+Bi]-C composite anode

(A–D) (A) The change in areal expansion during the first cycle. The data show the average areal expansion over three particles. The error bars represent standard deviations. TXM images of the [SnSb+Bi]-C composite anode at the (B) OCV, (C) full lithiation, and (D) delithiation states.

(e.g., Bi_2O_3-doped ZnO) and metallic alloys (e.g., Ni-doped W), where they are known to promote activated sintering and Coble creep.[37,56,57]

In interfacial thermodynamics, a liquid-like interfacial film of thickness h can be thermodynamically stabilized at a GB at $T < T_S$, if the volumetric free-energy penalty to form the undercooled liquid (ΔG^{vol}_{amorph}) can be over-compensated by the reduction in the interfacial energies upon replacing a "dry" GB (γ^0_{gb}) with two crystal-liquid interfaces ($2\gamma_{cl}$):[34–37]

$$\Delta G^{vol.}_{amorph} \cdot h < \gamma^0_{gb} - 2\gamma_{cl} \tag{1}$$

Following prior studies,[34–37] we can define a thermodynamic parameter

$$\lambda_0 \equiv \frac{\gamma^0_{gb} - 2\gamma_{cl}}{\Delta G^{(vol)}_{amorph}}, \tag{2}$$

where subscript "0" denotes that we adopt the bulk liquid composition at T_S as the liquid-like film composition in a simplification. This parameter λ_0 represents the thermodynamic ability to stabilize a liquid-like interfacial phase at an average general GB, and it scales the actual (equilibrium) interfacial width ($h_{eq.}$). Following the detailed procedure in Note S1, we calculated λ_0 versus temperature curve for a SnSb + 2.8 at% Bi alloy (noting that $\lambda_0(T)$ is a constant at a fixed temperature in the three-phase region), which is shown in Figure S13. Furthermore, a computed GB diagram is shown in Figure 2H, where red dashed lines (computed λ_0 values) are plotted in the bulk isopleth of SnSb + x at% Bi to represent the (upper bound of) estimated thickness of a liquid-like interfacial film that can be thermodynamically stabilized at an average general GB. The calculated λ_0 value of ~1.1 nm at room temperature suggests a liquid-like character of the Bi-enriched GB structure, which also has a Bi-enriched and Sb-depleted composition akin to the bulk liquid phase

(Figure 2G). Such a Bi-enriched, nanoscale, liquid-like interfacial phase can promote GB sliding and Coble creep to mitigate cracking during electrochemical cycling.

In a broader context, this nanoscale, liquid-like, interfacial phase represents one of segregation-based 2D interfacial phases that can form spontaneously as a thermodynamically equilibrium state (also named as "complexions"[54]) with composition and properties distinct from the corresponding bulk phase. Moreover, there are compositional and structural gradients in the through-thickness direction (Figure 2G), factors that are characteristic of GB complexions[54] that differentiate these 2D interfacial phases from thin precipitation layers of a 3D bulk phase.

In the current case, this Bi-enriched interfacial phase can help to improve cycling stability via two possible mechanisms. First, Bi segregation at GBs may stabilize the grain structure within the secondary particles during cycling. Second, its liquid-like character (analogous to segregation-induced interfacial premelting[58,59]) can promote GB sliding and Coble creep to release stress during cycling. Indeed, Sn-Bi alloys are known to exhibit superplasticity at room temperature due to GB sliding and enhanced Coble creep[31,32]. We hypothesize that a similar mechanism can prevail in SnSb-Bi alloys, which is supported by the interfacial thermodynamic modeling and cryo-STEM-EDS analysis (Figure 2).

During alloy type anode lithiation, mechanical stresses can induce crack formation.[60] Lithiation of alloy-type anodes usually involves multiple phase transformations, each of which has an associated volume expansion. For SnSb, lithiation results in the formation of Li_3Sb and various Li-Sn intermetallic compounds.[24] Abrupt Li concentration change generally exists at the phase boundary. With the volume expansion from the particle shell, the particle core region can experience compressive hoop stress, and the lithiated surface forms tensile hoop stress. Surface fractures occur when the accumulated stress exceeds the yield strength of the material.[61,62] Various factors can affect stress evolution, including Li-ion diffusion coefficients, current densities, and electrode particle geometry, as indicated by both experimental studies and computational models.[7,60,61]

On the other hand, it is known that low GB sliding resistance and high GB diffusion coefficients can enable Coble creep.[31,63,64] For the Sn-Bi alloys, for example, Bi GB sliding is facile even at room temperature due to the high GB diffusion coefficient (estimated to be 6.23×10^{-21} m^3s^{-1} for Bi GBs, and 3.15×10^{-21} m^3s^{-1} for Sn GBs).[31] Similar effects can exist in the SnSb-Bi GBs due to the formation of the liquid-like interfacial phase (Figure 2). For lithiation of high volumetric expansion anode, GBs are also subjected to stress; GB sliding and Coble creep have been reported as one of the mechanisms for stress relaxation.[61,65] In the current work, the dense SnSb+Bi anode can achieve better cycling stability with less porosity and a larger mean grain size in comparison with the more porous SnSb anode with smaller grains. The cycled SnSb+Bi anode also showed less severe surface bulges and cracks after cycling based on postcycling SEM and TXM characterization. This observation suggests the Bi segregation at GBs can stabilize microstructure upon cycling. Here, we further hypothesize that the Bi-enriched, nanoscale, interfacial phase at the SnSb GBs can also assist GB sliding and Coble creep, akin to Sn-Bi.[31] The strain energy could be released via GB sliding and Coble creep to alleviate GB stress concentration. A similar hypothesis of stress relief mechanism via GB sliding was also previously proposed for 3Ag-0.5Cu-96.5Sn-alloy-type anodes[65] and cobalt boride modified $LiNi_{0.8}Co_{0.1}Mn_{0.1}O_2$ cathodes[66] (but without direct evidence). For SnSb-Bi, this hypothesized mechanism is supported by interfacial thermodynamic modeling and a careful cryo-STEM-EDS analysis, along with the *in operando* TXM characterization.

While bulk Bi is known to lithiate at 0.8 V, there is also a possibility that the Bi-enriched interfacial phase can be lithiated. Yet, the formation of any crystalline Bi-Li intermetallic compound would likely increase the interfacial energy so that it may be suppressed (in comparison with the lower energy liquid-like interfacial phase). Further detailed GB characterization after cycling is needed to clarify this issue.

In a broader context, this study supports an emerging approach of thermodynamics-driven interfacial engineering via spontaneous formation of 2D interfacial phases (complexions).[67–70] These 2D interfacial phases are different from thin layers of 3D bulk phases in that they have a thermodynamically determined self-limiting thickness (~1 nm in this case), and they can form spontaneously. Both liquid-like[71–73] and ordered[59,67,74] GB complexions have been reported in various ceramic and metallic materials, including solid electrolytes and battery systems.[28,69] Analogous nanoscale surface phases with self-selecting thickness have also been used previously to improve battery performance,[28,75,76] and this study further suggests a new route to engineer GBs in alloy-type anodes (potentially extendable to other volume expansion materials).

Here, we investigate a thermodynamically controlled method to tailor the stability of the alloy-type anode. The spontaneous formation of a 2D liquid-like interfacial phase induced by Bi segregation was used to modify the GBs in an SnSb anode as an exemplar. This was achieved via a facile ball milling and annealing method. Both cryogenic STEM HAADF imaging and EDX elemental mapping revealed Bi enrichment at SnSb GBs. Our modeling showed that a nanoscale, Bi-enriched, liquid-like, interfacial phase can be thermodynamically stabilized at general GBs. The Bi-containing electrode showed improved cycling stability and rate capability compared to a pure SnSb electrode, despite the fact that the Bi-containing material is both denser (~99% dense particles) and shows larger primary grain sizes within comparable secondary particles. A specific capacity of 565.5 mAh/g was maintained for SnSb+Bi carbon composite electrode after 200 cycles, which corresponds to an 85.9% capacity retention. Postcycling SEM, 3D TXM, and *in operando* 2D TXM all demonstrate that the Bi GB modification significantly suppressed intergranular cracking upon lithiation and delithiation. In addition to stabilizing GBs, the nanometer-thick, Bi-enriched, interfacial phase may facilitate GB sliding and Coble creep to alleviate stress and avoid fracture upon cycling. This work thus suggests thermodynamically driven interfacial engineering of GBs as a new approach to improve the performance of battery electrode materials, particularly volume expansion anodes.

EXPERIMENTAL PROCEDURES

Resource availability

Lead contact

Further information and requests for resources and materials should be directed to and will be fulfilled by the lead contact, Jian Luo (jluo@alum.mit.edu).

Materials availability

All the materials generated in this study are available from the lead contact, Jian Luo (jluo@alum.mit.edu), upon request.

Data and code availability

All data is provided in the article and supplemental information or is available for the corresponding authors upon request.

Sample preparation

The alloy anodes were prepared using planetary ball milling. To fabricate alloyed particles of SnSb (without carbon), Sn (Alfa Aesar, 99.80%, 325 mesh) and Sb (Alfa Aesar, 99.5%, 200 mesh) in 1:1 mol ratio (total 4.809 g) were placed into a 100 mL yttrium stabilized zirconium oxide (YSZ) grinding jar with seven 10-mm and 50 3-mm YSZ grinding balls inside an Ar filled glovebox. The milling process was conducted for 8 h (48 cycles of 10 min each, with resting of 5 min in between) with an Across International PQ-N04 planetary ball mill at room temperature. To fabricate SnSb+Bi, 5 wt% Bi (Alfa Aesar, 99.999%, 200 mesh) was added, and the rest of the recipe is identical. To make [SnSb]-C and [SnSb+Bi]-C carbon composites (in a second step), 6.2 wt% graphite was added into the alloyed particles made via the above steps and subsequently milled for another 16 h (96 cycles of 10 min each, with resting of 5 min in between). To achieve a thermodynamic equilibrium, the milled powder was placed in a covered alumina crucible and isothermally annealed at 250°C (ramped with 5°C/min heating rate) for 3 h in a tube furnace in an Ar atmosphere. For the dense SnSb pellet with 2.8 at% of Bi, the ball milled powders (Sn and Bi in 1:1 mol ration with 5 wt% Bi) were uniaxially pressed in a stainless-steel die and placed in a covered alumina crucible and isothermally annealed at 250°C (ramped with 5°C/min heating rate) for 12 h in a tube furnace in an Ar atmosphere. The sintered pellet was polished before characterization.

Materials characterization

The alloy anodes were characterized by X-ray diffraction (XRD) with a Bruker D2 Phaser (Cu Kα radiation, λ = 1.5406 angstroms). To fabricate transmission electron microscopy (TEM) sample, a dual-beam focused ion beam FIB/SEM system (FEI Scios) was used to lift-out lamella. The powder grain structure was characterized with cryogenic TEM using a JEOL JEM-2800 microscope operated at 200 kV. SnSb+Bi alloy particles can be melted under room temperature with electron beam exposure. Thus, a liquid N_2 cooling holder (Gatan 626) was used to cool the TEM samples to around −170°C to minimize beam damage. Transmission X-ray Microscopy (TXM) was conducted at the Stanford Synchrotron Radiation Lightsource (SSRL) on beamline 6-2C. 8.95 KeV X-rays were utilized to characterize the particle morphology. The alloy particles were placed in a quartz tube and sealed with epoxy in an Ar filled glovebox. The tomography data were taken over an angular range of 180°. X-ray images were processed using TXM-Wizard.[77]

Electrochemical characterization

70 wt.% ball milled alloy powders were mixed with 15 wt% carbon fibers (Sigma-Aldrich) and 15 wt% carboxymethyl cellulose (CMC, MTI Corp) in DI water. Such a relatively high conductive carbon content was typically used for high-volume-change alloy-type anode materials to accommodate the volume expansion. Future optimization of active material-binder-conductive carbon ratio is required to increase electrode active material content. For *in situ* TXM experiment, an electrode with low active material loading (25 wt% active, 56 wt% carbon fiber, and 19 wt% CMC) were used to prevent particles overlapping. The slurry was mixed using a Thinky mixer (ARE-310) for 2 h at 2000 rpm. The slurry was coated on a copper foil (9 μm thick, MTI Corp) with a doctor blade, dried first in air for 12 h, and subsequently dried further at 80°C for 12 h in vacuum. The active material mass loading of the electrode was ~1.5 mg/cm^2. The electrode was not calendared after casting. Cycling tests were carried out with Li metal anode (excess amount, ~0.6 mm thick, ~16 mm diameter) and Celgard 2320 separator using 2032 coin cell. Two 0.5 mm thick spacer and one spring was used during coin cell assembly, and the total mass for the assembled coin cell is around 13 g. For *in situ* TXM characterization, Li metal pouch cells were

assembled in an argon filled glovebox. 1 M $LiPF_6$ in a 1:1 ethylene carbonate/diethyl carbonate solvent (LP40, Sigma-Aldrich) with 5 vol% fluorinated ethylene carbonates (FEC, Sigma-Aldrich) was used as the electrolyte (excess amount was used). Constant current cycling was conducted in a potential range of 0.05 – 1.5 V versus Li/Li^+ under ~20°C room temperature. The specific capacities were calculated based on the 70 wt.% active material to be around 660 mAh/g at 100 mA/g current density. Assuming ~250% volume expansion, the volumetric capacity of SnSb+Bi carbon composite anode can be calculated to be around 1790 Ah/L. The gravimetric stack energy was estimated using the model reported by Obrovac et al.[3] By using the $LiCoO_2$ (LCO) as baseline cathode with 530 Ah/L volumetric capacity, 1.1 N/P ratio, SnSb+Bi carbon composite anode average voltage of 0.75V, the stack energy can be calculated to be around 850 Wh/L. This corresponds to at least 17% increase compared to LCO/graphite cell (calculated to be 726 Wh/L using the same model).

SUPPLEMENTAL INFORMATION

Supplemental information can be found online at https://doi.org/10.1016/j.xcrp.2021.100694.

ACKNOWLEDGMENTS

This work is supported as part of the Center for Synthetic Control Across Length-scales for Advancing Rechargeables (SCALAR), an Energy Frontier Research Center funded by the United States Department of Energy, Office of Science, Basic Energy Sciences under Award No. DE-SC0019381. Use of the Stanford Synchrotron Radiation Light source, SLAC National Accelerator Laboratory, is supported by the U.S. Department of Energy, Office of Science, Office of Basic Energy Sciences, under Contract No. DE-AC02-76SF00515. The authors acknowledge the use of shared TEM facility at the UC Irvine Materials Research Institute (IMRI), which is supported in part by the National Science Foundation through the UC Irvine Materials Research Science and Engineering Center (UCI MRSEC DMR-2011967), as well as the Nano3/SDNI and IMCF facilities and instrumentation supported by the National Science Foundation (ECCS-1542148 and UCSD MRSEC DMR-2011924) at UC San Diego for specimen preparation.

AUTHOR CONTRIBUTIONS

J.L. and Q.Y. conceived the idea and designed the materials and experiments. Q.Y., S.T.K., G.W., and Y.Z. conducted the electrochemical testing. Q.Y., A.D., D.A.B., J.N.W., and S.H.T. performed the TXM experiments and analyses. Q.Y. performed the SEM, XRD, and TEM experiments and analyses. J.L., Q.Y., and M.Q. conducted the interfacial thermodynamic modeling and CALPHAD calculations. J.L. supervised and managed the overall research, and S.H.T., B.S.D., and J.N.W. supervised different areas of the work. All authors contributed to the discussion and provided comments on the manuscript.

DECLARATION OF INTERESTS

The authors declare no competing interests.

Received: September 1, 2021
Revised: November 3, 2021
Accepted: November 23, 2021
Published: December 21, 2021

REFERENCES

1. Dunn, B., Kamath, H., and Tarascon, J.-M. (2011). Electrical Energy Storage for the Grid: A Battery of Choices. Science *334*, 928–935.
2. Armand, M., and Tarascon, J.-M. (2008). Building better batteries. Nature *451*, 652–657.
3. Obrovac, M.N., and Chevrier, V.L. (2014). Alloy negative electrodes for Li-ion batteries. Chem. Rev. *114*, 11444–11502.
4. Park, C.M., Kim, J.H., Kim, H., and Sohn, H.J. (2010). Li-alloy based anode materials for Li secondary batteries. Chem. Soc. Rev. *39*, 3115–3141.
5. Cook, J.B., Detsi, E., Liu, Y., Liang, Y.L., Kim, H.S., Petrissans, X., Dunn, B., and Tolbert, S.H. (2017). Nanoporous Tin with a Granular Hierarchical Ligament Morphology as a Highly Stable Li-Ion Battery Anode. ACS Appl. Mater. Interfaces *9*, 293–303.
6. Yang, H., Fan, F., Liang, W., Guo, X., Zhu, T., and Zhang, S. (2014). A chemo-mechanical model of lithiation in silicon. J. Mech. Phys. Solids *70*, 349–361.
7. Huang, S., Fan, F., Li, J., Zhang, S., and Zhu, T. (2013). Stress generation during lithiation of high-capacity electrode particles in lithium ion batteries. Acta Mater. *61*, 4354–4364.
8. Sieradzki, K., Corderman, R.R., Shukla, K., and Newman, R.C. (1989). Computer simulations of corrosion: selective dissolution of binary alloys. Philos. Mag. A. *59*, 713–746.
9. Pickering, H.W., and Wagner, C. (1967). Electrolytic dissolution of binary alloys containing a noble metal. J. Electrochem. Soc. *114*, 698.
10. Chen, Q., and Sieradzki, K. (2013). Spontaneous evolution of bicontinuous nanostructures in dealloyed Li-based systems. Nat. Mater. *12*, 1102–1106.
11. Wagner, M.R., Raimann, P.R., Trifonova, A., Moeller, K.-C., Besenhard, J.O., and Winter, M. (2004). Electrolyte decomposition reactions on tin-and graphite-based anodes are different. Electrochem. Solid-State Lett. *7*, A201.
12. Park, A.R., and Park, C.M. (2017). Cubic Crystal-Structured SnTe for Superior Li- and Na-Ion Battery Anodes. ACS Nano *11*, 6074–6084.
13. Park, M.G., Lee, D.H., Jung, H., Choi, J.H., and Park, C.M. (2018). Sn-Based Nanocomposite for Li-Ion Battery Anode with High Energy Density, Rate Capability, and Reversibility. ACS Nano *12*, 2955–2967.
14. Lee, D.H., and Park, C.M. (2017). Tin Selenides with Layered Crystal Structures for Li-Ion Batteries: Interesting Phase Change Mechanisms and Outstanding Electrochemical Behaviors. ACS Appl. Mater. Interfaces *9*, 15439–15448.
15. Yan, Q., Ko, S.-T., Zhao, Y., Whang, G., Dawson, A., Tolbert, S., Dunn, B., and Luo, J. (2020). Cryogenic Milling Method to Fabricate Nanostructured Anodes. ACS Appl. Energy Mater. *3*, 11285–11292.
16. Cook, J.B., Lin, T.C., Detsi, E., Weker, J.N., and Tolbert, S.H. (2017). Using X-ray Microscopy To Understand How Nanoporous Materials Can Be Used To Reduce the Large Volume Change in Alloy Anodes. Nano Lett. *17*, 870–877.
17. Detsi, E., Petrissans, X., Yan, Y., Cook, J.B., Deng, Z., Liang, Y.L., Dunn, B., and Tolbert, S.H. (2018). Tuning ligament shape in dealloyed nanoporous tin and the impact of nanoscale morphology on its applications in Na-ion alloy battery anodes. Phys. Rev. Mater. *2*, 32–37.
18. Dalavi, S., Guduru, P., and Lucht, B.L. (2012). Performance enhancing electrolyte additives for lithium ion batteries with silicon anodes. J. Electrochem. Soc. *159*, A642.
19. Zhang, Q., Zhang, C., Luo, W., Cui, L., Wang, Y.-J., Jian, T., Li, X., Yan, Q., Liu, H., Ouyang, C., et al. (2020). Sequence-Defined Peptoids with -OH and -COOH Groups As Binders to Reduce Cracks of Si Nanoparticles of Lithium-Ion Batteries. Adv. Sci. (Weinh.) *7*, 2000749.
20. Philippe, B., Dedryvère, R., Gorgoi, M., Rensmo, H., Gonbeau, D., and Edström, K. (2013). Improved performances of nanosilicon electrodes using the salt LiFSI: a photoelectron spectroscopy study. J. Am. Chem. Soc. *135*, 9829–9842.
21. Zhang, J., and Xia, Y. (2006). Co-Sn alloys as negative electrode materials for rechargeable lithium batteries. J. Electrochem. Soc. *153*, A1466.
22. Yao, H., Zheng, G., Li, W., McDowell, M.T., Seh, Z., Liu, N., Lu, Z., and Cui, Y. (2013). Crab shells as sustainable templates from nature for nanostructured battery electrodes. Nano Lett. *13*, 3385–3390.
23. Kim, J.W., Ryu, J.H., Lee, K.T., and Oh, S.M. (2005). Improvement of silicon powder negative electrodes by copper electroless deposition for lithium secondary batteries. J. Power Sources *147*, 227–233.
24. Antitomaso, P., Fraisse, B., Stievano, L., Biscaglia, S., Aymé-Perrot, D., Girard, P., Sougrati, M.T., and Monconduit, L. (2017). SnSb electrodes for Li-ion batteries: the electrochemical mechanism and capacity fading origins elucidated by using operando techniques. J. Mater. Chem. A. *5*, 6546–6555.
25. Chao, S.C., Song, Y.F., Wang, C.C., Sheu, H.S., Wu, H.C., and Wu, N.L. (2011). Study on microstructural deformation of working Sn and SnSb anode particles for li-ion batteries by in situ transmission X-ray microscopy. J. Phys. Chem. C *115*, 22040–22047.
26. Kohandehghan, A., Cui, K., Kupsta, M., Memarzadeh, E., Kalisvaart, P., and Mitlin, D. (2014). Nanometer-scale Sn coatings improve the performance of silicon nanowire LIB anodes. J. Mater. Chem. A. *2*, 11261–11279.
27. Ye, J.C., An, Y.H., Heo, T.W., Biener, M.M., Nikolic, R.J., Tang, M., Jiang, H., and Wang, Y.M. (2014). Enhanced lithiation and fracture behavior of silicon mesoscale pillars via atomic layer coatings and geometry design. J. Power Sources *248*, 447–456.
28. Luo, J. (2019). Let thermodynamics do the interfacial engineering of batteries and solid electrolytes. Energy Storage Mater. *21*, 50–60.
29. Ohtani, H., and Ishida, K. (1994). A thermodynamic study of the phase equilibria in the Bi-Sn-Sb system. J. Electron. Mater. *23*, 747–755.
30. Manasijević, D., Vřešťál, J., Minić, D., Kroupa, A., Živković, D., and Živković, Ž. (2007). Phase equilibria and thermodynamics of the Bi–Sb–Sn ternary system. J. Alloys Compd. *438*, 150–157.
31. Wang, C.T., He, Y., and Langdon, T.G. (2020). The significance of strain weakening and self-annealing in a superplastic Bi–Sn eutectic alloy processed by high-pressure torsion. Acta Mater. *185*, 245–256.
32. Pearson, C.E. (1934). The viscous properties of extruded eutectic alloys of lead-tin and bismuth-tin. J. Inst. Materials. *54*, 111–124.
33. Campbell, C.E., Kattner, U.R., and Liu, Z.-K. (2014). File and data repositories for Next Generation CALPHAD. Scr. Mater. *70*, 7–11.
34. Zhou, N., and Luo, J. (2015). Developing grain boundary diagrams for multicomponent alloys. Acta Mater. *91*, 202–216.
35. Shi, X., and Luo, J. (2011). Developing grain boundary diagrams as a materials science tool: a case study of nickel-doped molybdenum. Phys. Rev. B Covering Condens. Matter Mater. Phys. *84*, 14105.
36. Luo, J., and Shi, X. (2008). Grain boundary disordering in binary alloys. Appl. Phys. Lett. *92*, 101901.
37. Luo, J. (2012). Developing interfacial phase diagrams for applications in activated sintering and beyond: current status and future directions. J. Am. Ceram. Soc. *95*, 2358–2371.
38. Jeurgens, L.P.H., Wang, Z., and Mittemeijer, E.J. (2009). Thermodynamics of reactions and phase transformations at interfaces and surfaces. Int. J. Mater. Res. *100*, 1281–1307.
39. Yang, K., Tang, J., Liu, Y., Kong, M., Zhou, B., Shang, Y., and Zhang, W.-H. (2020). Controllable Synthesis of Peapod-like Sb@C and Corn-like C@Sb Nanotubes for Sodium Storage. ACS Nano *14*, 5728–5737.
40. Liu, Z., Yu, X.Y., Lou, X.W., and Paik, U. (2016). Sb@C coaxial nanotubes as a superior long-life and high-rate anode for sodium ion batteries. Energy Environ. Sci. *9*, 2314–2318.
41. Guo, X., Xie, X., Choi, S., Zhao, Y., Liu, H., Wang, C., Chang, S., and Wang, G. (2017). Sb 2 O 3/MXene (Ti 3 C 2 T x) hybrid anode materials with enhanced performance for sodium-ion batteries. J. Mater. Chem. A. *5*, 12445–12452.
42. Sengupta, S., Mitra, A., Dahiya, P.P., Kumar, A., Mallik, M., Das, K., Majumder, S.B., and Das, S. (2017). Investigation on lithium conversion behavior and degradation mechanisms in Tin based ternary component alloy anodes for lithium ion batteries. J. Alloys Compd. *721*, 236–248.
43. Xie, J., Song, W., Zheng, Y., Liu, S., Zhu, T., Cao, G., and Zhao, X. (2011). Preparation and Li-storage properties of SnSb/graphene hybrid nanostructure by a facile one-step solvothermal route. Int. J. Smart Nano Mater. *2*, 261–271.

44. Yuan, Z., Wang, L., Wang, G., Yang, Z., Dong, L., and Yu, X. (2021). Composites of SnSb Nanoparticles Embedded in Porous Carbon Nanofibers Wrapped with Reduced Graphene Oxide for Sodium Storage. ACS Appl. Nano Mater. *4*, 826–833.

45. Du, Z., Jiang, Z., and Guo, C. (2006). Thermodynamic optimizing of the Li–Sn system. Int. J. Mater. Res. *97*, 10–16.

46. Okamoto, H. (2000). Phase Diagrams for Binary Alloys, Second Edition (ASM international).

47. Huggins, R.A. (1999). Lithium alloy negative electrodes. J. Power Sources *81*, 13–19.

48. Dahn, J.R., Courtney, I.A., and Mao, O. (1998). Short-range Sn ordering and crystal structure of Li4. 4Sn prepared by ambient temperature electrochemical methods. Solid State Ion. *111*, 289–294.

49. Kim, T., Choi, W., Shin, H.-C., Choi, J.-Y., Kim, J.M., Park, M.-S., and Yoon, W.-S. (2020). Applications of voltammetry in lithium ion battery research. J. Electrochem. Sci. Technol. *11*, 14–25.

50. Bard, A.J., and Faulkner, L.R. (2000). Electrochemical Methods: Fundamentals and Applications, Second Edition (John Wiley & Sons).

51. Wang, J., Fan, F., Liu, Y., Jungjohann, K.L., Lee, W., Mao, S.X., Liu, X., and Zhu, T. (2014). Structural Evolution and Pulverization of Tin Nanoparticles during Lithiation-Delithiation Cycling. J. Electrochem. Soc. *161*, F3019–F3024.

52. Weker, J.N., Liu, N., Misra, S., Andrews, J.C., Cui, Y., and Toney, M.F. (2014). In situ nanotomography and operando transmission X-ray microscopy of micron-sized Ge particles. Energy Environ. Sci. *7*, 2771–2777.

53. Clarke, D.R. (1987). On the equilibrium thickness of intergranular glass phases in ceramic materials. J. Am. Ceram. Soc. *70*, 15–22.

54. Dillon, S.J., Tang, M., Carter, W.C., and Harmer, M.P. (2007). Complexion: A new concept for kinetic engineering in materials science. Acta Mater. *55*, 6208–6218.

55. Luo, J. (2007). Stabilization of nanoscale quasi-liquid interfacial films in inorganic materials: a review and critical assessment. Crit. Rev. Solid State Mater. Sci. *32*, 67–109.

56. Luo, J., Wang, H., and Chiang, Y.-M. (1999). Origin of solid-state activated sintering in Bi2O3-Doped ZnO. J. Am. Ceram. Soc. *82*, 916–920.

57. Gupta, V.K., Yoon, D.-H., Meyer, H.M., III, and Luo, J. (2007). Thin intergranular films and solid-state activated sintering in nickel-doped tungsten. Acta Mater. *55*, 3131–3142.

58. Dash, J.G. (1989). Thermomolecular pressure in surface melting: motivation for frost heave. Science *246*, 1591–1593.

59. Yu, Z., Cantwell, P.R., Gao, Q., Yin, D., Zhang, Y., Zhou, N., Rohrer, G.S., Widom, M., Luo, J., and Harmer, M.P. (2017). Segregation-induced ordered superstructures at general grain boundaries in a nickel-bismuth alloy. Science *358*, 97–101.

60. Mukhopadhyay, A., and Sheldon, B.W. (2014). Deformation and stress in electrode materials for Li-ion batteries. Prog. Mater. Sci. *63*, 58–116.

61. Zhang, S., Zhao, K., Zhu, T., and Li, J. (2017). Electrochemomechanical degradation of high-capacity battery electrode materials. Prog. Mater. Sci. *89*, 479–521.

62. McDowell, M.T., Lee, S.W., Nix, W.D., and Cui, Y. (2013). 25th anniversary article: Understanding the lithiation of silicon and other alloying anodes for lithium-ion batteries. Adv. Mater. *25*, 4966–4985.

63. Shariat, P., Vastava, R.B., and Langdon, T.G. (1982). An evaluation of the roles of intercrystalline and interphase boundary sliding in two-phase superplastic alloys. Acta Metall. *30*, 285–296.

64. Hubert, P.J., Kathiresan, K., and Wakabayashi, K. (2011). Filler exfoliation and dispersion in polypropylene/as-received graphite nanocomposites via cryogenic milling. Polym. Eng. Sci. *51*, 2273–2281.

65. Xu, H., Li, S., Chen, X., Zhang, C., Liu, W., Fan, H., Yu, Y., Huang, Y., and Li, J. (2019). Sn-Alloy Foil Electrode with Mechanical Prelithiation: Full-Cell Performance up to 200 Cycles. Adv. Energy Mater. *9*, 1902150.

66. Yoon, M., Dong, Y., Hwang, J., Sung, J., Cha, H., Ahn, K., Huang, Y., Kang, S.J., Li, J., and Cho, J. (2021). Reactive boride infusion stabilizes Ni-rich cathodes for lithium-ion batteries. Nat. Energy *6*, 362–371.

67. Tang, M., Carter, W.C., and Cannon, R.M. (2006). Grain boundary transitions in binary alloys. Phys. Rev. Lett. *97*, 075502.

68. Cantwell, P.R., Tang, M., Dillon, S.J., Luo, J., Rohrer, G.S., and Harmer, M.P. (2014). Grain boundary complexions. Acta Mater. *62*, 1–48.

69. Luo, J. (2015). Interfacial engineering of solid electrolytes. J. Mater. *1*, 22–32.

70. Yan, Q., Whang, G., Wei, Z., Ko, S.-T., Sautet, P., Tolbert, S.H., Dunn, B.S., and Luo, J. (2020). A Perspective on interfacial engineering of lithium metal anodes and beyond. Appl. Phys. Lett. *117*, 80504.

71. Kayyar, A., Qian, H., and Luo, J. (2009). Surface adsorption and disordering in LiFePO 4 based battery cathodes. Appl. Phys. Lett. *95*, 221905.

72. Kang, B., and Ceder, G. (2009). Battery materials for ultrafast charging and discharging. Nature *458*, 190–193.

73. Hu, T., Yang, S., Zhou, N., Zhang, Y., and Luo, J. (2018). Role of disordered bipolar complexions on the sulfur embrittlement of nickel general grain boundaries. Nat. Commun. *9*, 2764.

74. Luo, J., Cheng, H., Asl, K.M., Kiely, C.J., and Harmer, M.P. (2011). The role of a bilayer interfacial phase on liquid metal embrittlement. Science *333*, 1730–1733.

75. Huang, J., Liu, H., Zhou, N., An, K., Meng, Y.S., and Luo, J. (2017). Enhancing the ion transport in $LiMn_{1.5}Ni_{0.5}O_4$ by altering the particle Wulff shape via anisotropic surface segregation. ACS Appl. Mater. Interfaces *9*, 36745–36754.

76. Huang, J., and Luo, J. (2014). A facile and generic method to improve cathode materials for lithium-ion batteries via utilizing nanoscale surface amorphous films of self-regulating thickness. Phys. Chem. Chem. Phys. *16*, 7786–7798.

77. Liu, Y., Meirer, F., Williams, P.A., Wang, J., Andrews, J.C., and Pianetta, P. (2012). TXM-Wizard: a program for advanced data collection and evaluation in full-field transmission X-ray microscopy. J. Synchrotron Radiat. *19*, 281–287.